

Formation of High-Performance Multi-Cation Halide Perovskites Photovoltaics by δ -CsPbI₃/ δ -RbPbI₃ Seed-Assisted Heterogeneous Nucleation

Essa A. Alharbi, Thomas P. Baumeler, Anurag Krishna, Ahmed Y. Alyamani, Felix T. Eickemeyer, Olivier Ouellette, Linfeng Pan, Fahad S. Alghamdi, Zaiwei Wang, Mohammad Hayal Alotaibi, Bowen Yang, Masaud Almalki, Mounir D. Mensi, Hamad Albrithen, Abdulrahman Albadri, Anders Hagfeldt, Shaik M. Zakeeruddin, and Michael Grätzel*

The performance of perovskite solar cells is highly dependent on the fabrication method; thus, controlling the growth mechanism of perovskite crystals is a promising way towards increasing their efficiency and stability. Herein, a multi-cation halide composition of perovskite solar cells is engineered via the two-step sequential deposition method. Strikingly, it is found that adding mixtures of 1D polymorphs of orthorhombic δ -RbPbI₃ and δ -CsPbI₃ to the PbI₂ precursor solution induces the formation of porous mesostructured hexagonal films. This porosity greatly facilitates the heterogeneous nucleation and the penetration of FA (formamidinium)/MA (methylammonium) cations within the PbI₂ film. Thus, the subsequent conversion of PbI₂ into the desired multication cubic α -structure by exposing it to a solution of formamidinium methylammonium halides is greatly enhanced. During the conversion step, the δ -CsPbI₃ also is fully integrated into the 3D mixed cation perovskite lattice, which exhibits high crystallinity and superior optoelectronic properties. The champion device shows a power conversion efficiency (PCE) over 22%. Furthermore, these devices exhibit enhanced operational stability, with the best device retaining more than 90% of its initial value of PCE under 1 Sun illumination with maximum power point tracking for 400 h.


1. Introduction

Over the last decade, organic–inorganic halide perovskite solar cells (PSCs) have garnered significant attention. Their high carrier mobility and long electron–hole diffusion length, small exciton binding energy, tunable bandgap, high absorption coefficient, and tolerance to defects make these materials suitable for a broad range of applications, ranging from photovoltaic devices to light-emitting diodes and lasers.^[1–5] Recently, certified power conversion efficiencies (PCE) of PSCs have reached 25.5%.^[6–13] The chemical formula ABX₃ of organic–inorganic halide perovskites stands for a monovalent A cation, that is, methylammonium (MA⁺ = CH₃NH₃⁺), formamidinium (FA⁺ = CH(NH₂)₂⁺), or Cs⁺ and Rb⁺, a divalent metal B cation (Pb²⁺, Ge²⁺, and Sn²⁺), and a halide anion X (I[−], Br[−], and Cl[−]). Tuning the perovskite bandgap and

E. A. Alharbi, T. P. Baumeler, Dr. F. T. Eickemeyer, Dr. O. Ouellette, M. Almalki, Dr. S. M. Zakeeruddin, Prof. M. Grätzel
Laboratory of Photonics and Interfaces
Institute of Chemical Sciences and Engineering
School of Basic Sciences
Ecole Polytechnique Fédérale de Lausanne
Lausanne CH-1015, Switzerland
E-mail: michael.graetzel@epfl.ch

Dr. A. Krishna, Dr. L. Pan, Dr. Z. Wang, Dr. B. Yang, Prof. A. Hagfeldt
Laboratory of Photomolecular Science
Institute of Chemical Sciences and Engineering
School of Basic Sciences Ecole Polytechnique Fédérale de Lausanne
Lausanne CH-1015, Switzerland

Prof. A. Y. Alyamani, F. S. Alghamdi, Dr. M. H. Alotaibi,
Dr. A. Albadri, Dr. H. Albrithen
National Center for Nanotechnology King Abdulaziz City
for Science and Technology
Riyadh 11442, Saudi Arabia

 The ORCID identification number(s) for the author(s) of this article can be found under <https://doi.org/10.1002/aenm.202003785>.

Dr. M. D. Mensi
Institute of Chemical Sciences and Engineering (ISIC)
École Polytechnique Fédérale de Lausanne
Sion CH-1950, Switzerland

Dr. H. Albrithen
K. A. CARE Energy Research and Innovation Center at Riyadh
Riyadh, Saudi Arabia

Dr. H. Albrithen
King Abdullah Institute for Nanotechnology-Aramco
Laboratory for Applied Sensing Research
King Saud University
Riyadh 11451, Saudi Arabia

Dr. H. Albrithen
Research Chair for Tribology, Surface, and Interface Sciences
Department of Physics and Astronomy
College of Science
King Saud University
Riyadh 11451, Saudi Arabia

Prof. A. Hagfeldt
Department of Chemistry – Ångström Laboratory
Uppsala University
Box 523, Uppsala 751 20, Sweden

DOI: 10.1002/aenm.202003785

modulating the crystallinity by using elemental composition engineering in bulk or at the surface via incorporation of multiple A cations and halides improves their performance and stability.^[7,14–17] Perovskite films are commonly fabricated using different techniques such as the one-step method (antisolvent), two-steps method (sequential deposition), thermal evaporation, vapor-assisted deposition, and blade coating.^[18–22] In the case of the antisolvent method, a certain amount of non-polar solvent is dripped on the perovskite precursor solution during spin-casting to initiate the nucleation and subsequent crystal growth of the perovskite. Achieving high reproducibility using this method is challenging, especially for large-area devices.^[23] In contrast, sequential deposition starts first with the deposition of an inorganic component, such as PbI_2 , not soluble in alcohol solvents, followed by the coating of a layer of organic salts, which interact with the inorganic component, leading to their final conversion into a perovskite film. This has been demonstrated as an effective method to fabricate dense and uniform perovskite films and devices with a high PCE and is considered a reliable strategy to upscale devices to large modules' size, owing to the better quality and higher reproducibility.^[19,24–27] One of the most promising perovskite composition is α -FAPbI₃ due to its broader light absorption range with its reduced bandgap.^[28,29] However, the perovskite cubic α -phase of FAPbI₃ is only thermodynamically stable above 400 K and turns into a yellow non-perovskite hexagonal phase (δ -phase) at room temperature.^[30] It was found that the incorporation of smaller cations (such as MA^+ , Cs^+ , and rubidium (Rb^+))^[7,14,16] or additives (such as phenylethylammonium (PEA^+), butylammonium (BA^+), and methylammonium chloride (MACl))^[31–34] leads to more stable devices with improved PCEs. Cs/FA double cations-based perovskites have the potential to stabilize the perovskite phase and increase the thermal and moisture stability due to the contraction of the cuboctahedral volume.^[35–37] For example, additives such as PEA^+ , BA^+ , MACl , or Rb^+ were found to work as stabilizers or crystallization aids that preserve the desirable photoactive perovskite α -phase of FAPbI₃ while improving the phase crystallinity and film quality.^[38–40]

However, for the sequential deposition method, it is difficult to introduce Cs^+ or Rb^+ in the FAPbI₃ lattice due to the low solubility of CsX and/or RbX ($\text{X} = \text{I}, \text{Br}, \text{or Cl}$) salts in alcohol solvents. This prevents adding these salts together with MA/FA cations in the second step of the process, which employs typically isopropanol (IPA) to dissolve the A cation halide. There have been few reports of the incorporation of Cs^+ in the perovskite fabricated with sequential deposition where either CsI or δ -CsPbI₃ phase was added to PbI_2 ^[41,42] which leads to perovskites with high crystallinity, excellent optoelectronic properties, and high performance. However, to the best of our knowledge, Rb^+ or Cs^+/Rb^+ mixtures so far have not been employed in the sequential deposition processes for the formation of perovskite films.

Herein, we report the systematic investigation of the role of multication-halide formulations in directing sequential deposition. For the first time, we examine the influence of δ -RbPbI₃ and δ -CsPbI₃ 1D polymorphs on the heterogeneous nucleation and conversion via the sequential deposition method and show the beneficial effect of quadruple cation formulation (RbCs-MAFA) on the conversion of PbI_2 films into perovskite. The introduction of a mixture of δ -RbPbI₃ and δ -CsPbI₃ 1D polymorphs induces the formation of a porous microstructure in

the PbI_2 films, which facilitates the penetration of the A cations into the PbI_2 and leads to its rapid and complete conversion into the photoactive α -phase perovskite.

2. Results and Discussion

We employed 1.15 M solution of PbI_2 in 1 mL of dimethylformamide (DMF) and 200 μL of dimethyl sulfoxide (DMSO) as a starting solution. To this we added either 7 mol% RbPbI_3 or 10 mol% CsPbI_3 or a mixture both, that is, 10 mol% CsPbI_3 and 7 mol% RbPbI_3 from 1.15 M stock solutions of RbPbI_3 and CsPbI_3 in DMSO (see Supporting Information for experimental details). We label these solutions as $\text{PbI}_2 \cdot 7\% \text{RbPbI}_3$, $\text{PbI}_2 \cdot 10\% \text{CsPbI}_3$, and $\text{PbI}_2 \cdot (7\% \text{RbPbI}_3 + 10\% \text{CsPbI}_3)$, respectively. We used these solutions during the first step of the sequential deposition to impregnate mesoporous TiO_2 layers and annealed them at 80 °C for 2–3 min. After letting the films cool down to room temperature, we exposed them during the second step of our sequential perovskite preparation to the organic halide salts (52.2 mg FAI, 5.2 mg MABr, and 5.2 mg MACl) dissolved in 1 mL isopropanol (IPA) and annealed them at 100 °C for 10 min and thereafter at 150 °C for 20 min. Here, methyl ammonium chloride (MACl) was used as an additive to improve the perovskite crystallization which sublimed during the annealing of the perovskite. The optimized compositions for the double, triple, and quadruple A-cation perovskites are $\text{FA}_{0.91}\text{MA}_{0.09}\text{Pb}(\text{I}_{0.91}\text{Br}_{0.09})_3$, $\text{Rb}_{0.07}\text{FA}_{0.85}\text{MA}_{0.08}\text{Pb}(\text{I}_{0.92}\text{Br}_{0.08})_3$, $\text{Cs}_{0.09}\text{FA}_{0.83}\text{MA}_{0.08}\text{Pb}(\text{I}_{0.92}\text{Br}_{0.08})_3$, and $\text{Rb}_{0.06}\text{Cs}_{0.08}\text{FA}_{0.78}\text{MA}_{0.08}\text{Pb}(\text{I}_{0.92}\text{Br}_{0.08})_3$, and these are labeled below as Control, Target-Rb, Target-Cs, and Target-RbCs, respectively. We present details on our optimization procedure in Figures S2–S5, Supporting Information. Humidity plays a key role in the nucleation and crystallization process of organic–inorganic perovskites as it activates the reaction of PbI_2 species with the halides.^[43] Hence, the perovskite films were annealed under an ambient atmosphere with a relative humidity (RH) of 30±5%. Also, processing under RH of 30±5% leads to a compact polycrystalline texture with full surface coverage and large grain size, features that are distinct from the small grain size and pinholes obtained from the films that were processed at a low humidity of 8±4% (Figure S6, Supporting Information). This is explained by the fact that the presence of water facilitates the ionic dissociation of FAI/MABr and thus accelerates the reaction of PbI_2 with the halides.^[43] Furthermore, processing conditions are known to be critical to yield highly reproducible PSCs, especially using the sequential deposition method as they impact the morphology of the PbI_2 precursor films, which is of crucial importance for the efficiency and stability of the final PSCs.^[44,45] Employing 30±5% RH, our method allows for producing highly efficient PSCs with very good reproducibility. We additionally found that optimizing the thickness of the mesoporous layer plays a key role in the conversion of PbI_2 into the perovskite (Figure S7, Supporting Information).

To understand the effect of δ -CsPbI₃ and δ -RbPbI₃ on the perovskite nucleation and growth we investigated the optical behavior of their precursor solutions. Figures 1a and 1d show their absorption spectra in solution and after deposition as solid films. Addition of the δ -RbPbI₃ and δ -CsPbI₃ polymorphs to the PbI_2 precursor solutions produces a small red shift of their

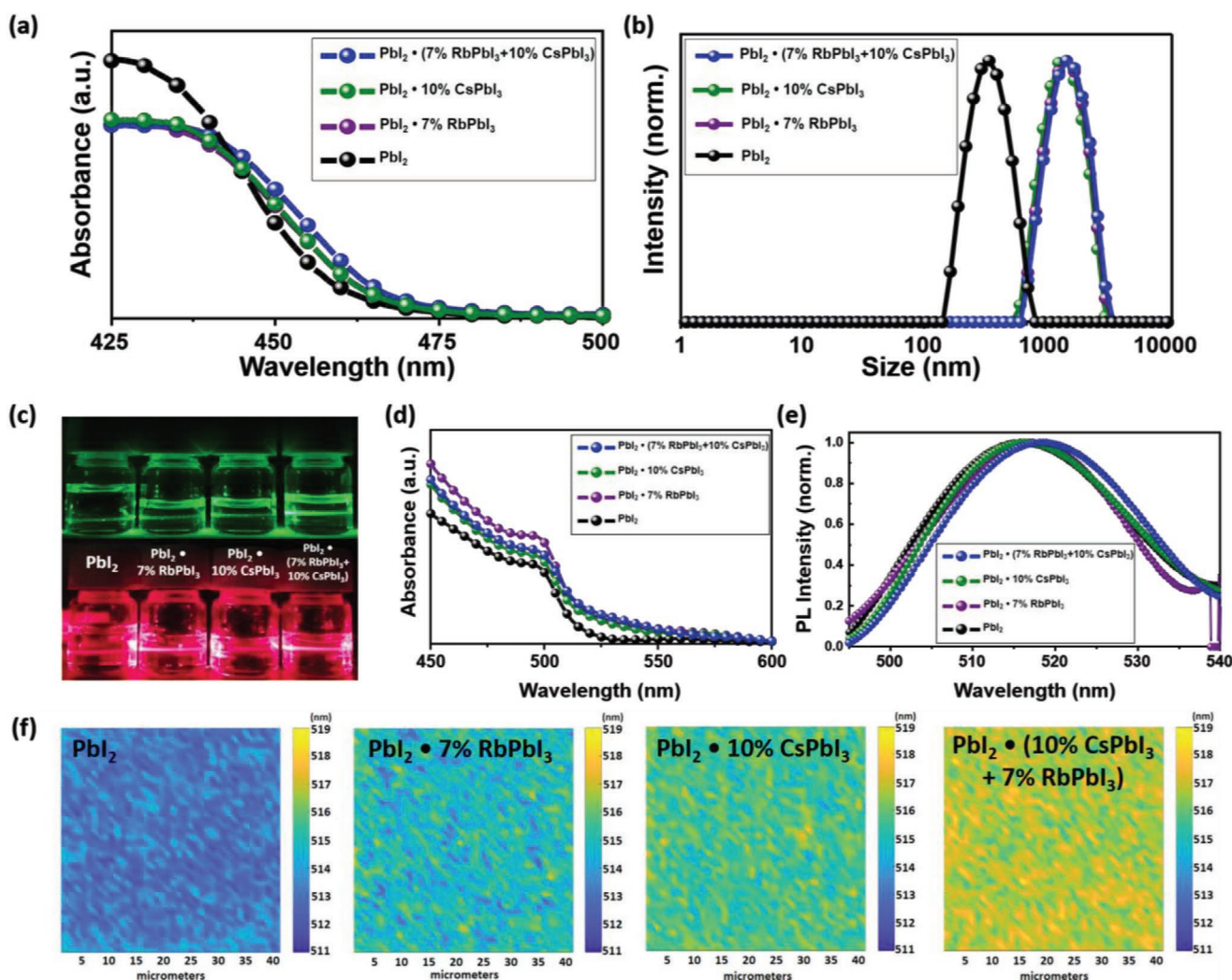


Figure 1. a) UV-Vis spectra, b) dynamic light scattering spectra, and c) Tyndall effect of PbI_2 , $\text{PbI}_2 \cdot 7\% \text{RbPbI}_3$, $\text{PbI}_2 \cdot 10\% \text{CsPbI}_3$, and $\text{PbI}_2 \cdot 7\% \text{RbPbI}_3 + 10\% \text{CsPbI}_3$ precursor perovskite solutions, respectively. d) UV-Vis spectra of the same condition as films and e) corresponding photoluminescence spectra and f) PL mapping of PbI_2 , $\text{PbI}_2 \cdot 7\% \text{RbPbI}_3$, $\text{PbI}_2 \cdot 10\% \text{CsPbI}_3$, and $\text{PbI}_2 \cdot 7\% \text{RbPbI}_3 + 10\% \text{CsPbI}_3$ films, respectively.

absorption and emission spectrum as well as a tail in the absorbance attributed to light scattering. Previous studies showed that perovskite precursors form colloids in the mother solution.^[46,47] The tailing of the absorbance towards longer wavelengths is likely to be caused by the formation of colloids with increased diameter. To gain further insight, we employed dynamic light scattering (DLS) measurements (Figure 1b and Figure S1a,b, Supporting Information), which confirmed the presence of colloids in the precursor solutions, the PbI_2 particles having a size of ≈ 350 nm. Upon the addition of the 7% RbPbI_3 , 10% CsPbI_3 , or (7% $\text{RbPbI}_3 + 10\% \text{CsPbI}_3$) precursor solutions the PbI_2 colloids disappear and larger colloids of microscopic size (1480 nm) are observed. Furthermore, we confirmed the colloidal nature of the precursor solutions by observing the Tyndall effect in solutions illuminated with laser beams of red and green wavelengths as shown in Figure 1c. We then performed photoluminescence (PL) mapping measurements on solid films prepared from the precursor solutions. The results shown in Figure 1f, reveal the persistence of colloidal particles in the intermediate phase PbI_2 films. The absorbance and

photoluminescence of all these intermediate phase films red-shift upon the addition of RbPbI_3 and/or CsPbI_3 , showing the same trend as for the solutions (Figure 1d,e). We investigated the structure and the morphology of the perovskite and non-perovskite precursor films using X-ray diffraction (XRD) and scanning electron microscopy (SEM).

The XRD patterns of the PbI_2 films with and without the 7% RbPbI_3 , 10% CsPbI_3 , and (7% $\text{RbPbI}_3 + 10\% \text{CsPbI}_3$) are shown in Figure 2a. The existence of 1D polymorphs of $\delta\text{-CsPbI}_3$ phase in PbI_2 layer after the introduction of 10% CsPbI_3 can be observed at 25.5° . Figure 2a also shows some peaks at 21.5° , 24.6° , 25.2° , and 25.6° belonging to 1D orthorhombic RbPbI_3 ($\text{PbI}_2 \cdot 7\% \text{RbPbI}_3$). The same peaks are observed for the mixture of (7% $\text{RbPbI}_3 + 10\% \text{CsPbI}_3$) together with the appearance of extra peaks at 25.5° and 28.8° belonging to the orthorhombic phase of CsPbI_3 .^[48–55] It should be noted that the PbI_2 peak at 12.5° , which belongs to the (001) lattice phase of hexagonal (2H polytype) of PbI_2 ^[56] is preserved in all compositions.

The XRD patterns of the corresponding perovskite films are shown in Figure 2b and Figures S8a, S9a, and S10a,

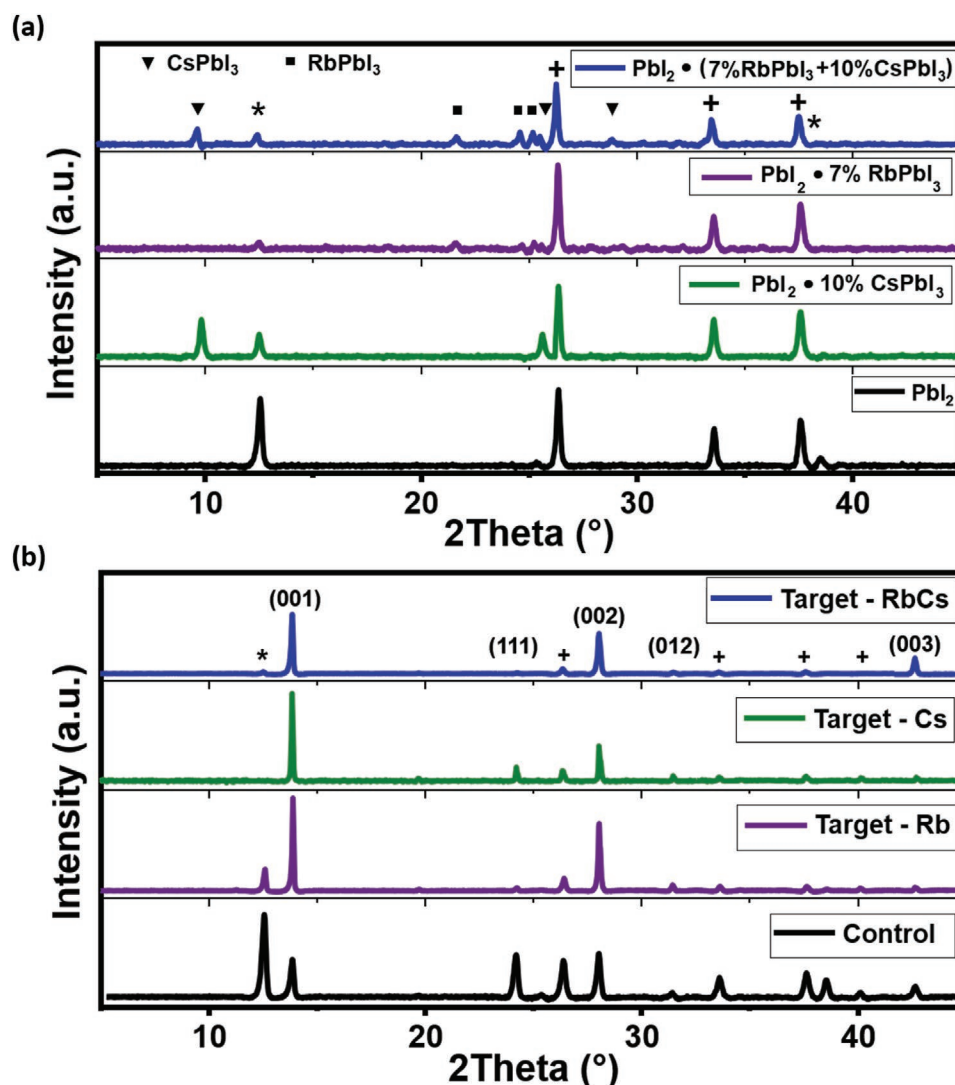


Figure 2. XRD patterns of a) non-perovskite for PbI_2 , $\text{PbI}_2 \cdot 7\% \text{RbPbI}_3$, $\text{PbI}_2 \cdot 10\% \text{CsPbI}_3$, and $\text{PbI}_2 \cdot 7\% \text{RbPbI}_3 + 10\% \text{CsPbI}_3$ films, respectively, (peaks marked with * and + are those assigned to PbI_2 and the FTO substrate, respectively) and b) Control, Target-Rb, Target-Cs, and Target-RbCs perovskite films.

Supporting Information. The patterns of perovskites for the Control films reveal the presence of unreacted PbI_2 at 12.5° , whereas the PbI_2 peak was not observable for the Target-Cs and Target-RbCs perovskites (Figures S8a, S9a, and S10a, Supporting Information). The suppression of the unreacted PbI_2 peak indicates that Target-Cs and Target-RbCs indeed underwent complete conversion and exhibit enhanced crystallinity. Furthermore, the surface and cross-section morphology of the intermediate phase (first step) and of the final perovskite phase films on mesoporous TiO_2 was investigated via SEM. Top-view and cross-section SEM images of the PbI_2 film without and with various inorganic non-perovskite dopings are shown in Figure 3a,b and Figures S8b, S9b, and S10b, Supporting Information. The pristine PbI_2 and $\text{PbI}_2 \cdot 7\% \text{RbPbI}_3$ film show a compact morphology, while the $\text{PbI}_2 \cdot 10\% \text{CsPbI}_3$ and $\text{PbI}_2 \cdot (10\% \text{CsPbI}_3, 7\% \text{RbPbI}_3)$ films exhibit a high degree of porosity and formation of nanorods. Previous work attributes the nanorods in the $\text{PbI}_2 \cdot 10\% \text{CsPbI}_3$ films to $\delta\text{-CsPbI}_3$.^[57] The cross-section of $\text{PbI}_2 \cdot 7\% \text{CsPbI}_3$ and $\text{PbI}_2 \cdot (10\% \text{CsPbI}_3, 7\% \text{RbPbI}_3)$

show mesoscopic porous structure in contrast to the compact to pristine PbI_2 and $\text{PbI}_2 \cdot 7\% \text{RbPbI}_3$ film. Such a mesoscopic network could be highly beneficial for facilitating the conversion of PbI_2 into the perovskite phase upon exposure to the organic salts.

The top-view SEM images of the perovskite films (Figure 3c) indicate that the presence of Cs^+ or a mixture of Cs^+/Rb^+ cations there generates a drastic increase in the grain size as well as an improvement in the homogeneity of the microstructure. This increase in grain size and phase purity indicates that the Target-Cs and Target-RbCs intermediate phases in the PbI_2 layer promote the growth of perovskite grains via the increase of the porosity of the PbI_2 films. The high porosity of PbI_2 films enables the efficient penetration of FA/MA cations and the subsequent conversion of the PbI_2 films into the cubic α perovskite structure in agreement with the XRD characterization. By comparison, in the Control and Target-Rb perovskite films, several residual unreacted PbI_2 particles are observable on the top of the perovskite layer, whereas there is no residual PbI_2 in the

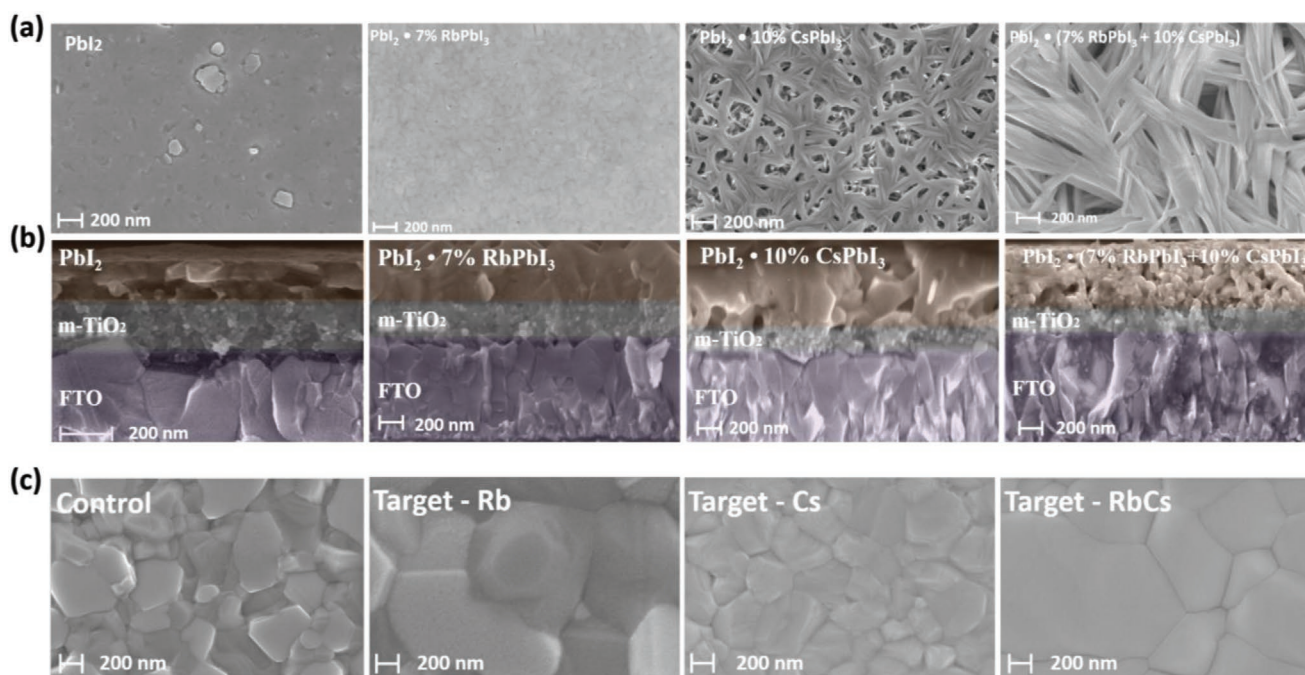


Figure 3. a) SEM top view and b) cross-sectional images for PbI_2 , $\text{PbI}_2 + 7\% \text{RbPbI}_3$, $\text{PbI}_2 + 10\% \text{CsPbI}_3$, and $\text{PbI}_2 + 7\% \text{RbPbI}_3 + 10\% \text{CsPbI}_3$ films, respectively, and c) SEM top view pictures for Control, Target-Rb, Target-Cs, and Target-RbCs perovskite film.

Target-Cs and Target-RbCs films. We concluded that the addition of $\delta\text{-CsPbI}_3$ / $\delta\text{-RbPbI}_3$ leads to a porous mesoscopic network, which facilitates the conversion into alpha perovskite leading to improved optoelectronic properties.

Figure 4a shows the absorbance spectra of Control, Target-Rb, Target-Cs, and Target-RbCs perovskite films. A blueshift is observed in the absorbance spectra upon CsPbI_3 incorporation. The incorporation of the smaller Cs^+ ions into the double cation crystal lattice reduces the effective radius of the triple cations ($\text{Cs}_x(\text{FA}_{0.91}\text{MA}_{0.09})_{1-x}$) as compared to double cations. As a result, the tolerance factor is driven towards a cubic lattice structure, and an increase in the optical bandgap is observed, which is consistent with previous work.^[14] However, the undoped Control perovskite and rubidium-doped (Target-Rb) perovskite

films show an unchanged absorbance onset (Figure 4a), which is in good agreement with previous reports,^[47,58,59] as Rb^+ ions are not incorporated into the perovskite lattice but rather act as film quality enhancer and/or surface passivation layer.^[60–64]

Relative steady-state photoluminescence (PL) photon flux spectra are shown in Figure 4b, measured in the same measurement geometry so that the relative intensities can be compared. The PL spectra show an emission peak at 1.53 eV for Control, and Target-Rb, while all Cs-containing compositions Target-Cs and Target-CsRb exhibit a blue-shifted emission (Figure 4b and Figures S8c, S9c, and S10c, Supporting Information). Furthermore, Target-Cs and Target-RbCs compositions show an emission peak at 1.55 eV, in agreement with the absorbance results as well as with external quantum efficiency (EQE) from the

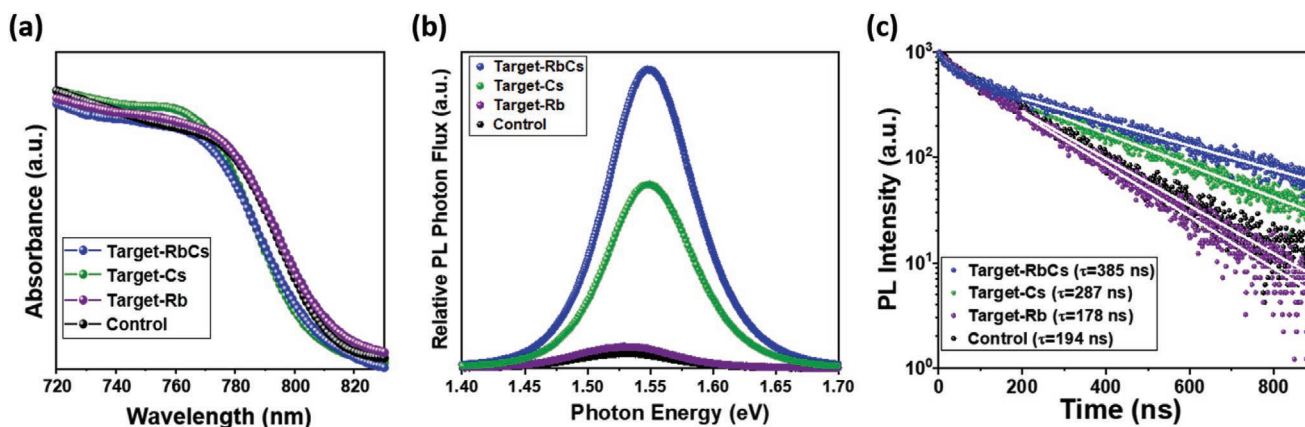


Figure 4. a) Absorbance spectrum, b) steady-state photoluminescence (PL), and c) time-resolved photoluminescence (TRPL) measurements of the different perovskite films, the solid lines are monoexponential fits for $t > 200$ ns.

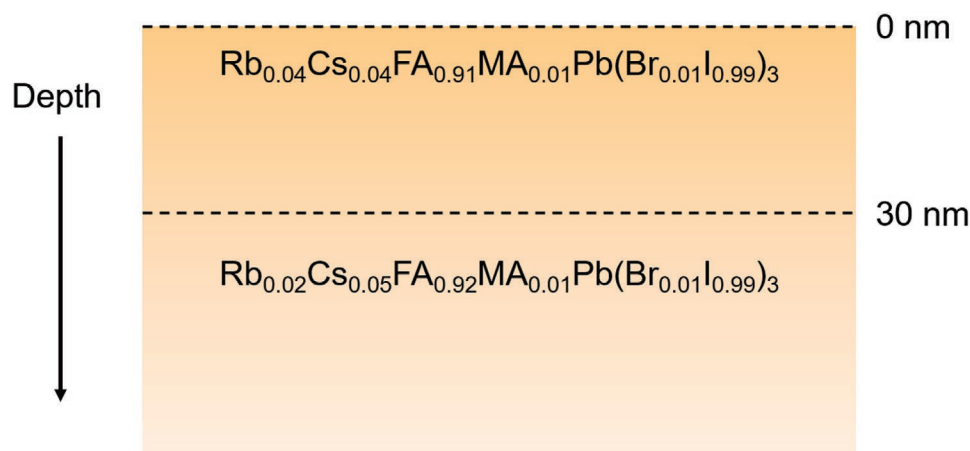


Figure 5. Scheme of the chemical composition at the surface and in the bulk of the perovskite layer from XPS measurement.

inflection point as shown in Figure S17, Supporting Information. Target-RbCs show the highest PL signal indicating the lowest non-radiative recombination rate, followed by Target-Cs, Target-Rb, and Control.

Next, we carried out time-resolved photoluminescence (TRPL) measurements to evaluate the charge carrier dynamics (Figure 4c) for Control, Target-Rb, Target-Cs, and Target-RbCs films. We performed our experiments at low fluences ($<5\text{ nJ cm}^{-2}$) so that bimolecular and Auger recombinations are negligible.^[65] All the TRPL traces show a monoexponential decay after $t > 200\text{ ns}$. This decay is due to non-radiative bulk and interface recombinations. We cannot distinguish between these two mechanisms with this TRPL experiment, but we can give an upper limit for the monomolecular bulk recombination constant k_1 assuming zero interface recombination velocity. In that way, the upper limits of k_1 for Control, Target-Rb, Target-Cs and Target-RbCs are $2.58 \times 10^6\text{ s}^{-1}$, $2.81 \times 10^6\text{ s}^{-1}$, $1.74 \times 10^6\text{ s}^{-1}$, and $1.3 \times 10^6\text{ s}^{-1}$, respectively. This suggests that there is a decrease in non-radiative recombination in Target-Cs and Target-RbCs perovskites, which is in good agreement with the steady-state PL measurements.

The elemental distribution of the composition with the longest carrier lifetime (Target-RbCs) was investigated using X-ray photoelectron spectroscopy (XPS). The XPS spectra (Figure 5 and Figures S11 and S12, Supporting Information) show that the elemental distribution differs between the surface (0 nm) and the bulk (30 nm) of the perovskite film (Table 1). As was expected,^[61,62,66,67] rubidium cations are not easily incorporated into the crystal lattice but rather preferentially act as surface defects passivation. In contrast to rubidium, the cesium cations are preferentially concentrated towards the bulk of the perovskite films. We note that the I/Br ratio is decreased to only $\approx 1\%$, which is in good agreement with the low bandgap of Target-RbCs (1.55 eV) estimated by PL and EQE measurements.

Table 1. Chemical composition at the surface and in the bulk of the perovskite layer determined by XPS.

Depth	Rb/Cs	Br/I	Cs/Pb	Chemical composition
0 nm	0.903	0.0085	0.04	$\text{Rb}_{0.04}\text{Cs}_{0.04}\text{FA}_{0.91}\text{MA}_{0.01}\text{Pb}(\text{Br}_{0.01}\text{I}_{0.99})_3$
30 nm	0.406	0.0077	0.06	$\text{Rb}_{0.02}\text{Cs}_{0.05}\text{FA}_{0.92}\text{MA}_{0.01}\text{Pb}(\text{Br}_{0.01}\text{I}_{0.99})_3$

Elemental ratios are summarized in Table 1 for the surface and the bulk. These results are consistent with previous reports.^[24,47,58,68–70]

To examine the photovoltaic performance of these perovskites, we fabricated complete devices in an FTO/c-TiO₂/mp-TiO₂/perovskite/spiro-OMeTAD/Au architecture (see Figures S13–S15, Supporting Information, for a comparison of all compositions). Figure 6a shows the cross-sectional SEM images of the full devices based on Control, Target-Cs, and Target-RbCs perovskites. The champion Control perovskite device shows a PCE of 20.42%, open-circuit voltage (V_{OC}) of 1.06 V, a short-circuit photocurrent (J_{SC}) of 24.30 mA cm^{-2} , and fill factor (FF) of 77%; the champion device for Target-Cs yields an enhanced PCE of 21.63%, with $V_{\text{OC}} = 1.12\text{ V}$, $J_{\text{SC}} = 24.80\text{ mA cm}^{-2}$, and FF of 78%, while Target-RbCs shows a PCE of 22.30%, J_{SC} of 24.82 mA cm^{-2} , $V_{\text{OC}} = 1.15\text{ V}$, and FF of 78% as shown in Figure 6b. The ideality factor n_{id} was extracted from the illumination intensity as a function of the V_{OC} (Figure S18, Supporting Information). The Control, Target-Cs, and Target-RbCs devices show a n_{id} of 1.56, 1.45, and 1.44, respectively. The improvement in V_{OC} is in coherence with the PL, TRPL, and ideality factor which shows suppression in non-radiative recombination. To the best of our knowledge, this is the highest efficiency to be achieved in RbCsFAMA-based PSCs fabricated via sequential deposition on a mesoscopic architecture.

The hysteresis for the best devices is shown in Figure S16, Supporting Information. In Target-Cs and Target-RbCs a small PCE difference between forward and reverse scans is observed, with hysteresis index ($\text{HI} = (PCE_{\text{backward}} - PCE_{\text{forward}})/PCE_{\text{backward}}$) of 0.07 and 0.02 respectively, whereas the Control device exhibits a higher hysteresis in current-voltage ($J-V$) scans with a HI of 0.13. The higher difference of hysteresis in the Control device is mainly due to the higher trap density in the perovskite film.^[7,14,61] Figure 6c shows the stabilized power output for the best performing devices during maximum power point tracking (MPP) in ambient air (10% RH (relative humidity)) under 1 Sun illumination for 130 sec. The stabilized PCE upon MPP tracking for Control, Target-Cs, and Target-RbCs are 19.5%, 21.2%, and 22.1%, respectively.

The incident photon-to-current efficiency (IPCE) spectra and integrated current density are shown in Figure 6d. In

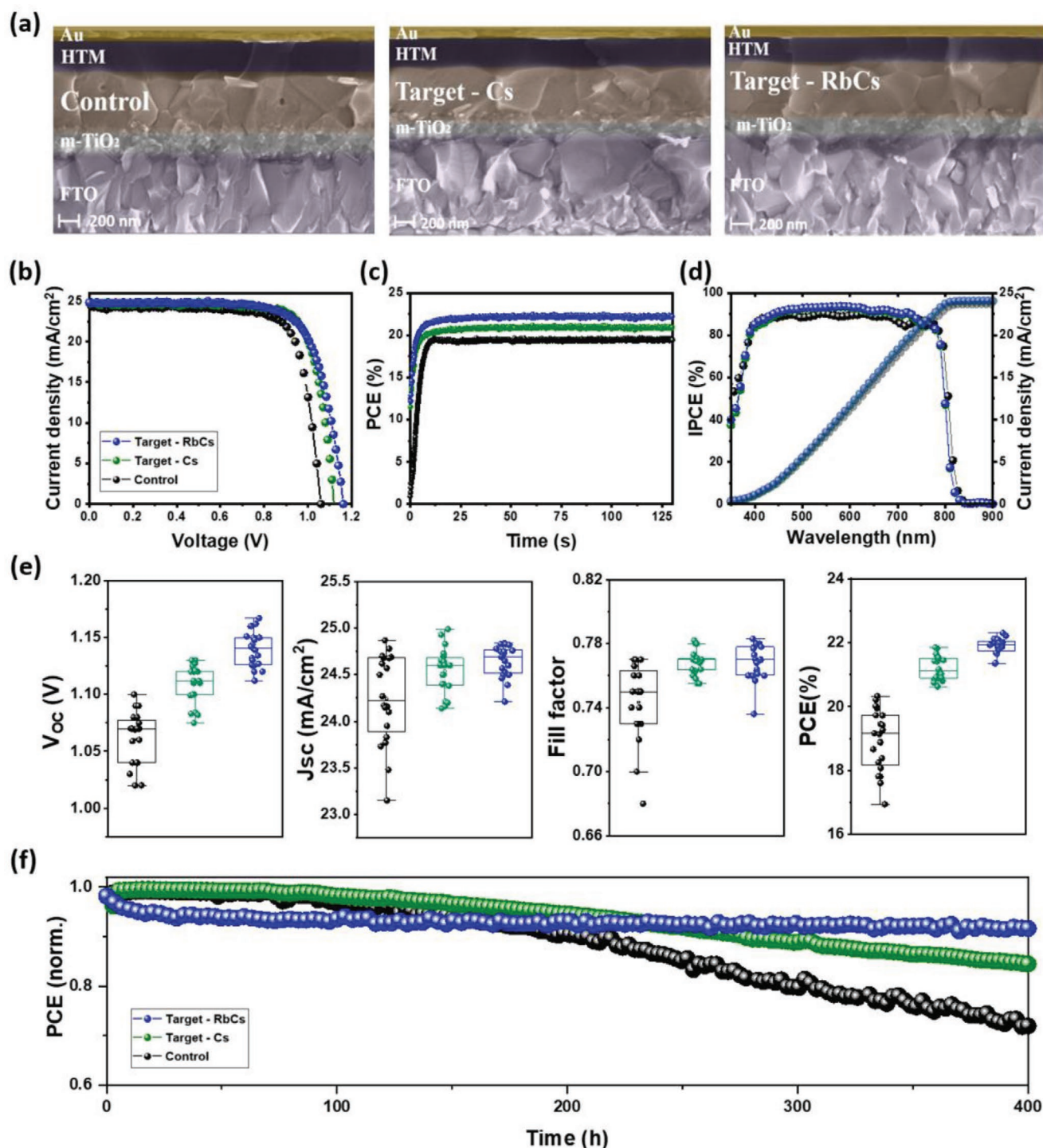


Figure 6. a) Cross-sectional SEM images, b) J–V curves of the devices, c) maximum power point tracking, d) IPCE spectra and photocurrent integrated over the standard AM 1.5G solar spectrum, e) J–V metrics of devices, and f) operational stability in a nitrogen environment at room temperature under continuous illumination (LED source, approximated 1 Sun) at maximum power point for Control, Target-Cs, and Target-RbCs.

agreement with absorbance spectra, a small blue shift in the onset of the IPCE spectra is detected for Target-Cs and Target-RbCs devices as compared to Control, while integrated current densities agree with the J_{SC} -values derived from the J–V measurements 24.04, 24.01, and 23.97 mA cm^{−2}. The statistical dis-

tribution of the photovoltaic characteristics (J_{SC} , V_{OC} , FF, and PCE) from at least 20 devices of each composition is presented in Figure 6e. The statistical distribution shows Target-Cs and Target-RbCs-based devices are much more reproducible than Control-based devices.

Operational stability remains a major concern in PSCs.^[69,70] Therefore, the devices based on Control, Target-Cs, and Target-RbCs were subjected to light soaking in simulated solar irradiation at their maximum power for 400 h under a nitrogen atmosphere at room temperature as shown in Figure 6f. Devices fabricated with Control, Target-Cs, and Target-RbCs perovskite retained $\approx 72\%$, $\approx 85\%$, and $\approx 92\%$ of the initial performance after 400 h, respectively. Shelf stability was monitored as well by keeping the devices at room temperature and at 30–55% RH for 400 h. As shown in Figure S19, Supporting Information, devices retained $\approx 55\%$, $\approx 70\%$, and $\approx 78\%$ for Control, Target-Cs, and Target-RbCs, respectively. This showed that our strategy to produce quadruple cation perovskite not only improves performance but also enhances the device stability.

3. Conclusion

In summary, we demonstrated the importance of the multi-cation halide composition engineering of PSCs fabricated by sequential deposition. Utilizing a mix of fully 1D inorganic photoinactive phase (δ -RbPbI₃/ δ -CsPbI₃) resulted in an improvement of the perovskite crystallization via the creation of a mesoscopic porous network in the PbI₂ film, which enabled the facilitated penetration of the A-cations into PbI₂ and the subsequent conversion into efficient α cubic photoactive perovskite structures. XPS revealed that rubidium cations are mostly located at the surface of the perovskite film as well as the ratio of MAPbBr₃ is decreased to only $\approx 1\%$, which is in good agreement with the low bandgap of Target-RbCs (1.55 eV) estimated by PL/EQE measurements. There is significant enhancement of the open-circuit voltage from 1.06 to 1.12 V, and 1.15 V, leading to a PCE of 20.42%, 21.63%, and 22.30% for Control, Target-Cs, and Target-RbCs, respectively. The Target-RbCs based device shows high operational stability and retains more than 90% of its initial PCE after 400 h illumination under MPP tracking. This work exemplifies the importance of tuning the crystallization in PSCs and has the potential to stimulate other successful developments in the future.

4. Experimental Section

Solar Cell Preparation: Fluorine-doped tin oxide (FTO)-glass substrates (TCO glass, NSG 10, Nippon sheet glass, Japan) were etched from the edges by using Zn powder and 4 M HCl and then, were cleaned by ultrasonication in Hellmanex (2%, deionized water), rinsed thoroughly with de-ionized water and ethanol, and then treated in oxygen plasma for 15 min. A 30 nm blocking layer (TiO₂) was deposited on the cleaned FTO by spray pyrolysis at 450 °C using a commercial titanium diisopropoxide bis(acetylacetonate) solution (75% in 2-propanol, Sigma-Aldrich) diluted in anhydrous ethanol (1:9 volume ratio) as precursor and oxygen as a carrier gas. A mesoporous TiO₂ layer was deposited by spin-coating a diluted paste in ethanol (1:6 wt. ratio) or (1:8.5 wt. ratio) or (1:10.5 wt. ratio) (Dyesol 30NRD: ethanol) (3000 rpm, acceleration 2000 rpm for 20 s) onto the substrate containing TiO₂ compact layer, and then sintered at 450 °C for 30 min in dry air.

Fabrication of Perovskite Films: 1.15 M PbI₂ or CsPbI₃ or RbPbI₃ or a mixture solution precursor were stirred at 70 °C for 12 h. PbI₂, PbI₂.x%CsPbI₃ (x = 0%, 5%, 10%, 15%, and 20%) or PbI₂.x%RbPbI₃ (x = 0%, 7%, 10%, 15%, and 20%) or PbI₂.x%CsPbI₃.y%RbPbI₃ (x = 10% and y = 0%, 7%, 10%, 15%, and 20%) solutions were spin-coated on

FTO/c-TiO₂/meso-TiO₂ substrate at 4000 r.p.m. for 45 s and then heated at 80 °C for 2–3 min to remove the solvents. After cooling down, the FAI/MABr/MACl mixture solution was spin-coated on top of the PbI₂ or PbI₂.x%CsPbI₃ or PbI₂.x%RbPbI₃ or a mixture of PbI₂.10%CsPbI₃.y%RbPbI₃ at 2500 r.p.m. for 45 s followed by annealing at 100 °C for 10 min and 150 °C for 20 min with a relative humidity $\approx 30 \pm 5\%$ to fabricate perovskite film. The HTM was deposited in by spin-coating at 4000 rpm for 30 s in a dry box with controlled humidity $\approx 8 \pm 4\%$. The HTM was doped with bis(trifluoromethylsulfonyl)imide lithium salt (17.8 μ l prepared by dissolving 520 mg LiTFSI in 1 ml of acetonitrile) and 28.8 μ l of 4-tert-butylpyridine. Finally, an ≈ 80 nm gold (Au) layer was thermally evaporated.

Device Characterization: The J–V characteristics of the perovskite devices were recorded with a digital source meter (Keithley model 2400, USA). A 450 W xenon lamp (Oriel, USA) was used as the light source for photovoltaic (J–V) measurements. The spectral output of the lamp was filtered using a Schott K113 Tempax sunlight filter (Präzisions Glas & Optik GmbH, Germany) to reduce the mismatch between the simulated and actual solar spectrum to less than 2%. The photo-active area of 0.16 cm² was defined using a dark-colored metal mask.

Incident Photon-to-Current Efficiency (IPCE): IPCE was recorded under a constant white light bias of ≈ 5 mW cm^{−2} supplied by an array of white light emitting diodes. The excitation beam coming from a 300 W Xenon lamp (ILC Technology) was focused through a Gemini-180 double monochromator (Jobin Yvon Ltd) and chopped at ≈ 2 Hz. The signal was recorded using a Model SR830 DSP Lock-In Amplifier (Stanford Research Systems).

Scanning Electron Microscopy (SEM): SEM was performed on a ZEISS Merlin HR-SEM.

X-ray Powder Diffractions: These were recorded on an X'Pert MPD PRO (Panalytical) equipped with a ceramic tube (Cu anode, $\lambda = 1.54060$ Å), a secondary graphite (002) monochromator and a RTMS X'Celerator (Panalytical).

UV–Vis Measurements (UV–Vis): UV–Vis were performed on a Varian Cary 5.

Photoluminescence Spectra (PL): PL were obtained with a Florolog 322 (Horiba Jobin Yvon Ltd) in the wavelength range from 500 to 850 nm by exciting at 460 nm.

Time-Resolved Photoluminescence (TRPL): TRPL was measured with FluoroLog-3 (Horiba) spectrometer working in a time-correlated single photon counting mode with a lower nanosecond time resolution. A picosecond pulsed diode laser head NanoLED N-670L (Horiba) emitting < 200 ps duration pulses at 670 nm with a maximum repetition rate of 1 MHz was used as excitation source.

Long Term Light Soaking Test: Stability measurements were performed with a Biologic MPG2 potentiostat under a full AM 1.5 Sun-equivalent white LED lamp. The devices were measured with a MPP tracking routine under continuous illumination at room temperature. The MPP was updated every 10 s by a standard perturb and observe method. Every minute a J–V curve was recorded in order to track the evolution of individual J–V parameters.

X-Ray Photoelectron Spectroscopy (XPS): XPS was carried out using a PHI VersaProbe II scanning XPS microprobe with Al K α X-ray source. The spherical capacitor analyzer was set at 45° take-off angle with respect to the sample surface. Bulk composition analysis was done after argon plasma etching. Data were processed using the PHI Multipak software.

Supporting Information

Supporting Information is available from the Wiley Online Library or from the author.

Acknowledgements

E.A. gratefully acknowledges King Abdulaziz City for Science and Technology (KACST) for a fellowship. T.B., M.G., and S.M.Z thank the King Abdulaziz City for Science and Technology (KACST) and the SNSF for the project

under JST-SNSF program (Grant No. IZJSZ2-180176) for the financial support. A.K. acknowledges funding from the European Union's Horizon 2020 Research and Innovation program under the Marie Skłodowska-Curie Grant Agreement No 843453. O.O. acknowledges funding from the Natural Sciences and Engineering Research Council of Canada. B.Y. acknowledges funding from the European Union's Horizon 2020 research and innovation programme under grant agreement No 764047.

Conflict of Interest

The authors declare no conflict of interest.

Author Contributions

E.A.A. and T.P.B. contributed equally to this work. E.A. and M.G. conceived the idea of the work. E.A. designed the experiment. E.A. and T.B. fabricated and optimized the solar cell devices. T.B. did the basic characterizations of perovskite films. T.B., Z.W., F.S.A., and B.Y. recorded the SEM and XRD measurements. M.H., M.A., and A.A. contributed in the device fabrication. L.P. recorded the XPS measurements. M.D.M. recorded the PL mapping measurements. O.O., T.B., and E.A. recorded the TRPL measurements. F.E. analyzed the TRPL data. A.K. helped with data analysis, manuscript revision, and recorded the stability measurements. E.A. and T.B. analyzed the results and wrote the manuscript. M.G., S.M.Z., and A.Y.A. supervised the project and discussed the results. All authors contributed to the edition of the manuscript. E.A. and T.B. contributed equally to this work.

Data Availability Statement

Research data are not shared.

Keywords

compositional engineering, Perovskite solar cells, stability, two step methods

Received: December 7, 2020

Revised: February 9, 2021

Published online: March 15, 2021

- [1] M. Liu, M. B. Johnston, H. J. Snaith, *Nature* **2013**, 501, 395.
- [2] H. Zhou, Q. Chen, G. Li, S. Luo, T. B. Song, H. S. Duan, Z. Hong, J. You, Y. Liu, Y. Yang, *Science* **2014**, 345, 542.
- [3] Q. Chen, H. Zhou, Z. Hong, S. Luo, H. S. Duan, H. H. Wang, Y. Liu, G. Li, Y. Yang, *J. Am. Chem. Soc.* **2014**, 136, 622.
- [4] M. A. Green, A. Ho-Baillie, H. J. Snaith, *Nat. Photonics* **2014**, 8, 506.
- [5] Y. Zhao, K. Zhu, *J. Phys. Chem. C* **2014**, 118, 9412.
- [6] G. Kim, H. Min, K. S. Lee, D. Y. Lee, S. M. Yoon, S. I. Seok, *Science* **2020**, 370, 108.
- [7] M. Saliba, T. Matsui, K. Domanski, J. Y. Seo, A. Ummadisingu, S. M. Zakeeruddin, J. P. Correa-Baena, W. R. Tress, A. Abate, A. Hagfeldt, M. Grätzel, *Science* **2016**, 354, 206.
- [8] Y. H. Lin, N. Sakai, P. Da, J. Wu, H. C. Sansom, A. J. Ramadan, S. Mahesh, J. Liu, R. D. J. Oliver, J. Lim, L. Aspirtarte, K. Sharma, P. K. Madhu, A. B. Morales-Vilches, P. K. Nayak, S. Bai, F. Gao, C. R. M. Grovenor, M. B. Johnston, J. G. Labram, J. R. Durrant, J. M. Ball, B. Wenger, B. Stannowski, H. J. Snaith, *Science* **2020**, 369, 96.
- [9] X. Zheng, Y. Hou, C. Bao, J. Yin, F. Yuan, Z. Huang, K. Song, J. Liu, J. Troughton, N. Gasparini, C. Zhou, Y. Lin, D. J. Xue, B. Chen, A. K. Johnston, N. Wei, M. N. Hedhili, M. Wei, A. Y. Alsalloum, P. Maity, B. Turedi, C. Yang, D. Baran, T. D. Anthopoulos, Y. Han, Z. H. Lu, O. F. Mohammed, F. Gao, E. H. Sargent, O. M. Bakr, *Nat. Energy* **2020**, 5, 131.
- [10] Y. Cao, N. Wang, H. Tian, J. Guo, Y. Wei, H. Chen, Y. Miao, W. Zou, K. Pan, Y. He, H. Cao, Y. Ke, M. Xu, Y. Wang, M. Yang, K. Du, Z. Fu, D. Kong, D. Dai, Y. Jin, G. Li, H. Li, Q. Peng, J. Wang, W. Huang, *Nature* **2018**, 562, 249.
- [11] K. Lin, J. Xing, L. N. Quan, F. P. G. de Arquer, X. Gong, J. Lu, L. Xie, W. Zhao, D. Zhang, C. Yan, W. Li, X. Liu, Y. Lu, J. Kirman, E. H. Sargent, Q. Xiong, Z. Wei, *Nature* **2018**, 562, 245.
- [12] Y. C. Kim, K. H. Kim, D. Y. Son, D. N. Jeong, J. Y. Seo, Y. S. Choi, I. T. Han, S. Y. Lee, N. G. Park, *Nature* **2017**, 550, 87.
- [13] A. Kojima, K. Teshima, Y. Shirai, T. Miyasaka, *J. Am. Chem. Soc.* **2009**, 131, 6050.
- [14] M. Saliba, T. Matsui, J. Y. Seo, K. Domanski, J. P. Correa-Baena, M. K. Nazeeruddin, S. M. Zakeeruddin, W. Tress, A. Abate, A. Hagfeldt, M. Grätzel, *Energy Environ. Sci.* **2016**, 9, 1989.
- [15] E. A. Alharbi, M. I. Dar, N. Arora, M. H. Alotaibi, Y. A. Alzhari, P. Yadav, W. Tress, A. Alyamani, A. Albadi, S. M. Zakeeruddin, M. Grätzel, *Research* **2019**, 2019, 8474698.
- [16] E. A. Alharbi, A. Y. Alyamani, D. J. Kubicki, A. R. Uhl, B. J. Walder, A. Q. Alanazi, J. Luo, A. Burgos-Caminal, A. Albadi, H. Albrithen, M. H. Alotaibi, J. E. Moser, S. M. Zakeeruddin, F. Giordano, L. Emsley, M. Grätzel, *Nat. Commun.* **2019**, 10, 3008.
- [17] S. Mahesh, J. M. Ball, R. D. J. Oliver, D. P. McMeekin, P. K. Nayak, M. B. Johnston, H. J. Snaith, *Energy Environ. Sci.* **2020**, 13, 258.
- [18] J. M. Kadro, K. Nonomura, D. Gachet, M. Grätzel, A. Hagfeldt, *Sci. Rep.* **2015**, 5, 11654.
- [19] J. Burschka, N. Pellet, S. J. Moon, R. Humphry-Baker, P. Gao, M. K. Nazeeruddin, M. Grätzel, *Nature* **2013**, 499, 316.
- [20] O. Malinkiewicz, A. Yella, Y. H. Lee, G. M. Espallargas, M. Grätzel, M. K. Nazeeruddin, H. J. Bolink, *Nat. Photonics* **2014**, 8, 128.
- [21] J. M. Ball, M. M. Lee, A. Hey, H. J. Snaith, *Energy Environ. Sci.* **2013**, 6, 1739.
- [22] J. H. Kim, S. T. Williams, N. Cho, C. C. Chueh, A. K. Y. Jen, *Adv. Energy Mater.* **2015**, 5, 1401229.
- [23] N. J. Jeon, J. H. Noh, Y. C. Kim, W. S. Yang, S. Ryu, S. I. Seok, *Nat. Mater.* **2014**, 13, 897.
- [24] W. S. Yang, J. H. Noh, N. J. Jeon, Y. C. Kim, S. Ryu, J. Seo, S. I. Seok, *Science* **2015**, 348, 1234.
- [25] J. H. Im, I. H. Jang, N. Pellet, M. Grätzel, N. G. Park, *Nat. Nanotechnol.* **2014**, 9, 927.
- [26] J. Seo, S. Park, Y. C. Kim, N. J. Jeon, J. H. Noh, S. C. Yoon, S. I. Seok, *Energy Environ. Sci.* **2014**, 7, 2642.
- [27] Y. Y. Kim, E. Y. Park, T. Y. Yang, J. H. Noh, T. J. Shin, N. J. Jeon, J. Seo, *J. Mater. Chem. A* **2018**, 6, 12447.
- [28] G. E. Eperon, S. D. Stranks, C. Menelaou, M. B. Johnston, L. M. Herz, H. J. Snaith, *Energy Environ. Sci.* **2014**, 7, 982.
- [29] Z. Li, M. Yang, J. S. Park, S. H. Wei, J. J. Berry, K. Zhu, *Chem. Mater.* **2016**, 28, 284.
- [30] N. J. Jeon, J. H. Noh, W. S. Yang, Y. C. Kim, S. Ryu, J. Seo, S. I. Seok, *Nature* **2015**, 517, 476.
- [31] J. W. Lee, Z. Dai, T. H. Han, C. Choi, S. Y. Chang, S. J. Lee, N. De Marco, H. Zhao, P. Sun, Y. Huang, Y. Yang, *Nat. Commun.* **2018**, 9, 3021.
- [32] H. S. Yoo, N. G. Park, *Sol. Energy Mater. Sol. Cells* **2018**, 179, 57.
- [33] G. Liu, H. Zheng, X. Xu, L. Zhu, A. Alsaedi, T. Hayat, X. Pan, S. Dai, *J. Mater. Chem. A* **2018**, 6, 18067.
- [34] T. Niu, J. Lu, M. C. Tang, D. Barrit, D. M. Smilgies, Z. Yang, J. Li, Y. Fan, T. Luo, I. McCulloch, A. Amassian, S. Liu, K. Zhao, *Energy Environ. Sci.* **2018**, 11, 3358.
- [35] C. Yi, J. Luo, S. Meloni, A. Boziki, N. Ashari-Astani, C. Grätzel, S. M. Zakeeruddin, U. Röthlisberger, M. Grätzel, *Energy Environ. Sci.* **2016**, 9, 656.
- [36] S. D. Stranks, H. J. Snaith, *Nat. Nanotechnol.* **2015**, 10, 391.
- [37] T. Liu, H. Lai, X. Wan, X. Zhang, Y. Liu, Y. Chen, *Chem. Mater.* **2018**, 30, 5264.

- [38] M. Kim, G. H. Kim, T. K. Lee, I. W. Choi, H. W. Choi, Y. Jo, Y. J. Yoon, J. W. Kim, J. Lee, D. Huh, H. Lee, S. K. Kwak, J. Y. Kim, D. S. Kim, *Joule* **2019**, 3, 2179.
- [39] T. Duong, H. K. Mulmudi, H. Shen, Y. L. Wu, C. Barugkin, Y. O. Mayon, H. T. Nguyen, D. Macdonald, J. Peng, M. Lockrey, W. Li, Y. B. Cheng, T. P. White, K. Weber, K. Catchpole, *Nano Energy* **2016**, 30, 330.
- [40] M. Zhang, J. S. Yun, Q. Ma, J. Zheng, C. F. J. Lau, X. Deng, J. Kim, D. Kim, J. Seidel, M. A. Green, S. Huang, A. W. Y. Ho-Baillie, *ACS Energy Lett.* **2017**, 2, 438.
- [41] N. Zhou, Y. Shen, Y. Zhang, Z. Xu, G. Zheng, L. Li, Q. Chen, H. Zhou, *Small* **2017**, 13, 1700484.
- [42] W. Zhou, Y. Cheng, K. Chen, G. Xie, T. Wang, G. Zhang, *Adv. Funct. Mater.* **2020**, 30, 2070048.
- [43] Y. Xu, L. Zhu, J. Shi, X. Xu, J. Xiao, J. Dong, H. Wu, Y. Luo, D. Li, Q. Meng, *ChemPhysChem* **2016**, 17, 112.
- [44] S. Pathak, A. Sepe, A. Sadhanala, F. Deschler, A. Haghighirad, N. Sakai, K. C. Goedel, S. D. Stranks, N. Noel, M. Price, S. Hüttner, N. A. Hawkins, R. H. Friend, U. Steiner, H. J. Snaith, *ACS Nano* **2015**, 9, 2311.
- [45] H. S. Ko, J. W. Lee, N. G. Park, *J. Mater. Chem. A* **2015**, 3, 8808.
- [46] K. Yan, M. Long, T. Zhang, Z. Wei, H. Chen, S. Yang, J. Xu, *J. Am. Chem. Soc.* **2015**, 137, 4460.
- [47] Y. Zhao, H. Tan, H. Yuan, Z. Yang, J. Z. Fan, J. Kim, O. Voznyy, X. Gong, L. N. Quan, C. S. Tan, J. Hofkens, D. Yu, Q. Zhao, E. H. Sargent, *Nat. Commun.* **2018**, 9, 1607.
- [48] M. H. Jung, S. H. Rhim, D. Moon, *Sol. Energy Mater. Sol. Cells* **2017**, 172, 44.
- [49] D.-H. Lim, P. Ramasamy, D.-H. Kwak, J.-S. Lee, *Nanotechnology* **2017**, 28, 255601.
- [50] T. Zhang, M. I. Dar, G. Li, F. Xu, N. Guo, M. Grätzel, Y. Zhao, *Sci. Adv.* **2017**, 3, e1700841.
- [51] Y. Wang, M. I. Dar, L. K. Ono, T. Zhang, M. Kan, Y. Li, L. Zhang, X. Wang, Y. Yang, X. Gao, Y. Qi, M. Grätzel, Y. Zhao, *Science* **2019**, 365, 591.
- [52] H. Meng, Z. Shao, L. Wang, Z. Li, R. Liu, Y. Fan, G. Cui, S. Pang, *ACS Energy Lett.* **2020**, 5, 263.
- [53] T. Burwig, W. Fränzel, P. Pistor, *J. Phys. Chem. Lett.* **2018**, 9, 4808.
- [54] D. M. Trots, S. V. Myagkota, *J. Phys. Chem. Solids* **2008**, 69, 2520.
- [55] B. Han, B. Cai, Q. Shan, J. Song, J. Li, F. Zhang, J. Chen, T. Fang, Q. Ji, X. Xu, H. Zeng, *Adv. Funct. Mater.* **2018**, 28, 1804285.
- [56] M. S. Mohammed, G. D. Salman, K. I. Hassoon, *Al-Mustansiriyah J. Sci.* **2019**, 30, 60.
- [57] X. Xu, M. Li, Y. M. Xie, Y. Ma, C. Ma, Y. Cheng, C. S. Lee, S. W. Tsang, *ACS Appl. Mater. Interfaces* **2019**, 11, 6126.
- [58] W. S. Yang, B. W. Park, E. H. Jung, N. J. Jeon, Y. C. Kim, D. U. Lee, S. S. Shin, J. Seo, E. K. Kim, J. H. Noh, S. I. Seok, *Science* **2017**, 356, 1376.
- [59] Q. Jiang, L. Zhang, H. Wang, X. Yang, J. Meng, H. Liu, Z. Yin, J. Wu, X. Zhang, J. You, *Nat. Energy* **2017**, 2, 16177.
- [60] D. J. Kubicki, D. Prochowicz, A. Hofstetter, S. M. Zakeeruddin, M. Grätzel, L. Emsley, *J. Am. Chem. Soc.* **2017**, 139, 14173.
- [61] P. Yadav, M. I. Dar, N. Arora, E. A. Alharbi, F. Giordano, S. M. Zakeeruddin, M. Grätzel, *Adv. Mater.* **2017**, 29, 1701077.
- [62] R. Uchida, S. Binet, N. Arora, G. Jacopin, M. H. Alotaibi, A. Taubert, S. M. Zakeeruddin, M. I. Dar, M. Graetzel, *Small* **2018**, 14, 1802033.
- [63] J. W. Lee, D. H. Kim, H. S. Kim, S. W. Seo, S. M. Cho, N. G. Park, *Adv. Energy Mater.* **2015**, 5, 1501310.
- [64] X. Xia, W. Wu, H. Li, B. Zheng, Y. Xue, J. Xu, D. Zhang, C. Gao, X. Liu, *RSC Adv.* **2016**, 6, 14792.
- [65] T. Kirchartz, J. A. Márquez, M. Stolterfoht, T. Unold, *Adv. Energy Mater.* **2020**, 10, 1904134.
- [66] M. Abdi-Jalebi, Z. Andaji-Garmaroudi, A. J. Pearson, G. Divitini, S. Cacovich, B. Philippe, H. Rensmo, C. Ducati, R. H. Friend, S. D. Stranks, *ACS Energy Lett.* **2018**, 3, 2671.
- [67] U.-G. Jong, C.-J. Yu, Y.-H. Kye, C.-H. Kim, S.-G. Ri, Y. Chen, *arXiv* **2018**.
- [68] B. Philippe, M. Saliba, J. P. Correa-Baena, U. B. Cappel, S. H. Turren-Cruz, M. Grätzel, A. Hagfeldt, H. Rensmo, *Chem. Mater.* **2017**, 29, 3589.
- [69] K. Domanski, E. A. Alharbi, A. Hagfeldt, M. Grätzel, W. Tress, *Nat. Energy* **2018**, 3, 61.
- [70] W. Tress, K. Domanski, B. Carlsen, A. Agarwalla, E. A. Alharbi, M. Graetzel, A. Hagfeldt, *Nat. Energy* **2019**, 4, 568.